NATO OTAN
Science & Technology Organization (STO)

The Relationship between Fatigue Life and the Microstructure and Mesostructure of Additively Manufactured Materials

Emiel Amsterdam, Ali Chabok
Royal Netherlands Aerospace Centre (NLR)
Voorsterweg 31, Marknesse
THE NETHERLANDS

emiel.amsterdam@nlr.nl

ABSTRACT

Topology optimization and novel manufacturing technologies like additive manufacturing (AM) have provided designers with the tools to manufacture highly optimized components. However, these components require an understanding of relationships between the microstructure and mesostructure of the materials from which they are built, and the performance in terms of fatigue. Many microstructure-property relationships focus on the relationship between the microstructure and the quasi-static mechanical properties. However, accurate physical models that relate the fatigue properties to the microstrucuture and mesostructure of materials such as metallic AM alloys are lacking. The current study focuses on the effect of the microstrucuture and mesostructure of additively manufactured materials on fatigue properties. In particular, a fracture-mechanics-informed phenomenological model is introduced that accurately describes the influence of the initial discontinuity size, the applied maximum cyclic stress, and the ultimate tensile strength on the high cycle fatigue life of AlSi10Mg and Ti-6Al-4V made by laser powder bed fusion. The effect of the mesostructure on load re-distribution and crack re-nucleation during fatigue loading was investigated using stretch-dominated multiple load path specimens of AlSi10Mg and Ti-6Al-4V that were tested in the as-built surface condition. The results show that the multiple load path structures are more damage tolerant, but have an overall lower fatigue life.

RESUME

L'optimisation topologique et les nouvelles technologies de fabrication, telles que la fabrication additive (FA), ont fourni aux concepteurs les outils nécessaires pour produire des composants hautement optimisés. Cependant, ces composants nécessitent une compréhension des relations entre la micro- et la méso-structure des matériaux à partir desquels ils sont fabriqués, ainsi que des performances en termes de fatigue. De nombreuses relations microstructure-propriété se concentrent sur le lien entre la microstructure et les propriétés mécaniques quasi-statiques. Toutefois, il manque des modèles physiques précis qui relient les propriétés en fatigue à la micro- et à la méso-structure des matériaux, comme les alliages métalliques issus de la FA. La présente étude se concentre sur l'effet de la micro- et de la méso-structure des matériaux fabriqués par fabrication additive sur les propriétés en fatigue. En particulier, un modèle phénoménologique basé sur la mécanique de la rupture est introduit, permettant de décrire avec précision l'influence de la taille initiale des discontinuités, de la contrainte cyclique maximale appliquée et de la résistance à la traction ultime sur la durée de vie en fatigue à grand nombre de cycles des alliages AlSi10Mg et Ti-6Al-4V fabriqués par fusion sur lit de poudre laser. L'effet de la méso-structure sur la re-distribution des charges et la re-nucléation des fissures lors du chargement en fatigue a été étudié à l'aide d'éprouvettes à chemins de charge multiples à dominante traction en AlSi10Mg et Ti-6Al-4V, testées dans leur état de surface tel que fabriqué. Les résultats montrent que les structures à chemins de charge multiples sont plus tolérantes aux dommages, mais présentent une durée de vie en fatigue globalement plus faible.

KEYWORDS

Additive manufacturing; Fatigue properties; Materials mesostructure; Topology optimization.

MILITARY RELEVANCE

Throughout history, technological advantage has often revolved around the development and utilization of advanced materials, and this remains true for modern military platforms. In the context of military platforms, manoeuvrability and performance are paramount, as they directly impact the effectiveness of military operations. AM is increasingly important for military platforms due to its potential to revolutionize the production of complex, light-weight components with added functionality and advanced alloys. To fully leverage the benefits of AM, understanding the relationship between microstructure, material properties and performance is crucial. By understanding these relationships, military engineers can design and optimize AM components for specific applications, enhancing their performance and survivability. Ultimately, mastering the connection between microstructure, material properties, and performance will be key to unlocking the full potential of AM in military platforms and maintaining a technological advantage on the battlefield.

1.0 INTRODUCTION

Topology optimization and novel manufacturing technologies like additive manufacturing (AM) have provided designers with tools to create highly optimized structures, as well as the ability to fabricate them. The introduction of Integrated Computational Materials Engineering (ICME) and hierarchical bioinspired architected materials require relationships between the micro- and mesostructure of materials and the performance of materials in terms of failure mechanisms (e.g., corrosion or fatigue). Many microstructure-property relationships focus on the relationship between the microstructure and the quasi-static mechanical properties. However, accurate physical models that relate the fatigue properties to the microstrucuture and mesostructure of materials such as metallic AM alloys, high entropy alloys, bioinspired architected materials or fibre reinforced materials are lacking. The current study focuses on the effect of the microstrucuture and mesostructure of additively manufactured AlSi10Mg and Ti-6Al-4V on the fatigue properties.

1.1 Microstructure and Discontinuities

Additive manufacturing can introduce defects into the microstructure, such as gas pores, lack of fusion (LoF) defects or oxides [1], [2]. Gas pores are inherent to the AM process and can therefore hardly be called defects. Hence, gas pores, LoF defects or other type of local stress concentrations will be referred to as discontinuities. The fatigue life of AM specimens very much depends on the stress fields surrounding the discontinuities. The stress in the material adjacent to the discontinuity depends on the far field applied stress and loading direction, the size and shape of the discontinuity, the distance to the surface and the proximity of other stress raisers [1], [2].

However, the fatigue life is also influenced by the microstructure and grain structure of the material adjacent to the discontinuity, because these factors determine short crack growth rates and the probability of high crack growth rates in the stress concentration adjacent to the discontinuity [3]. Additionally, the environment in which these small cracks are growing plays a role, because internal cracks that grow in a vacuum or an inert environment generally show lower crack propagation rates than surface cracks growing in (humid) air [2]. The roles of shape, distance to the surface, and the local grain structure are also reasons why the discontinuities with the largest cross-sectional area perpendicular to the loading direction do not always lead to failure of the specimen [4], [5].

Similarly, for a given shape and size of a discontinuity, the remaining influences still give rise to a distribution of fatigue lives for a certain maximum stress and stress ratio, due to differences in the microstructure, i.e. grain orientations and grain boundaries, surrounding the defect. This results in different small crack growth rates and, hence, a different fatigue lives [3], [4], [5], [6], [7].

On average, fatigue life decreases as the discontinuity increases for a given maximum stress [7], [8], [9]. A similar decrease in fatigue life with increasing discontinuity size was observed for corrosion pit depth in aluminium alloy 2024-T4, 7050-T7451, Q235 steel, 17-4PH and 12% Cr steam turbine blade steel [10], [11], [12], [13], [14], [15]. The fatigue lives and endurance limit of Jethete M152 steel also decreases with increasing corrosion pit depth and decreasing SiC grit finish [16]. However, this effect is less pronounced at higher stresses.

Similarly, the effect of surface finish on fatigue life is less pronounced at high stresses when forging steel with different hardnesses [17]. The extrapolated reversed bending S-N curves for as-forged and polished surface conditions intersect at $3.5 \cdot 10^3$ cycles for hardnesses of 19 and 35 HRC. The maximum stress at which the S-N curves intersect are 97% and 96% of the ultimate tensile strength (UTS) for 19 and 35 HRC, respectively [17]. For additively manufactured Ti-6Al-4V, the extrapolated R= -1 S-N curves for as-built and polished specimens also intersect near the UTS [18]. The stress at 1,000 cycles, S_{1000}, was used as a fixed point and a change in slope was used to characterise the decrease in fatigue life for the as-built condition for all tested maximum stresses [18].

The S_{1000} value for this Ti-6Al-4V that is made by laser powder bed fusion (L-PBF) are 893 MPa for the as-built material and 950 MPa for the polished material, both corresponding to 79% of the UTS [18]. The S_{1000} method is a well-known empirical method to account for surface finish in steels, where different slopes are used for different surface finish or roughness [17], [18], [19], [20]. For steel and R= -1, S_{1000} is about 75% of the UTS, and the endurance limit (S_e) is about 50% of the UTS [19], [20].

By decreasing S_e at 10^6 cycles with different factors for surface finish or specimen size, the slope between the fixed S_{1000} and S_e increases as S_e decreases. Apparently, the effect of corrosion pit depth and surface roughness are more pronounced at low stress and less pronounced at high stresses and this gives rise to a change in slope of the S-N curve. This is in contrast with the work by Murakami, et al. on the essential structure of the S-N curve, where changes to the slope are not considered for different discontinuity sizes [7].

A pivot point and a change in slope with a change in discontinuity size have been used in earlier work to model the effect of L-PBF defects in AlSi10Mg [21]. In that work the major axis of the discontinuity from which the fatigue crack nucleated was used as a metric for the size of the discontinuity. Murakami, et al. use the square root of the discontinuity area as a metric for the size of the fatigue crack nucleating feature [7], [8]. However, using a length equal to $\sqrt{area}$ implicitly assumes a square shape of the nucleating feature. David and Lazarus showed that the crack front, after nucleation from an irregular shape quickly becomes circular and its growth with the number of cycles can be obtained analytically using a circular crack of same area as the original irregular shape [22].

Essentially, replacing a complex crack front shape with a semi-circular configuration shape having equal area improves the ease of prediction. For a semi-circular surface crack the $\sqrt{area}$ is 1.25 times greater than the radius of the semi-circular surface crack. This results in a stress intensity factor that is $\sqrt{1.25} = 1.12$ times greater than the actual stress intensity factor of the semi-circular surface crack if the geometry factor is not changed. Thus, in this approach, each discontinuity is idealized as a semi-ellipse and the short and long axis of the ellipse are measured. From the semi-ellipse a semi-circle with equal area is determined and the radius of this equivalent semi-circle (r_{eq}) is used as a single metric for the size of the discontinuity. The equivalent radius is calculated as a function of the lengths of the semi-major and semi-minor axes:

$$r_{eq} = \sqrt{a \cdot c} \tag{1}$$

where a is the maximum depth measured from the surface and $2c$ the maximum width along the surface for a discontinuity at the surface (see Figure 1). Depending on the shape a can be either the semi-major axis or the semi-minor axis (and vice versa for c).

1.2 Mesostructure

Additionally, the mesostructure can affect the fatigue performance of hierarchical bioinspired architected materials made by additive manufacturing. For a given weight, an architected material can be additively manufactured using an increasing number of load paths with decreasing path thickness. The choice of the length scale of the architected material and, hence the number of load paths, affects the surface area, load re-distribution and crack re-nucleation during cyclic loading. To investigate the effects of load re-distribution and crack re-nucleation stretch-dominated multiple load path specimens of AlSi10Mg and Ti-6Al-4V were produced using laser powder bed fusion and tested in the as-built surface condition. For these types of specimens, the as-built surface condition was used, because post-process machining or surface roughness reduction is likely not possible or too time-consuming for high-complexity applications.

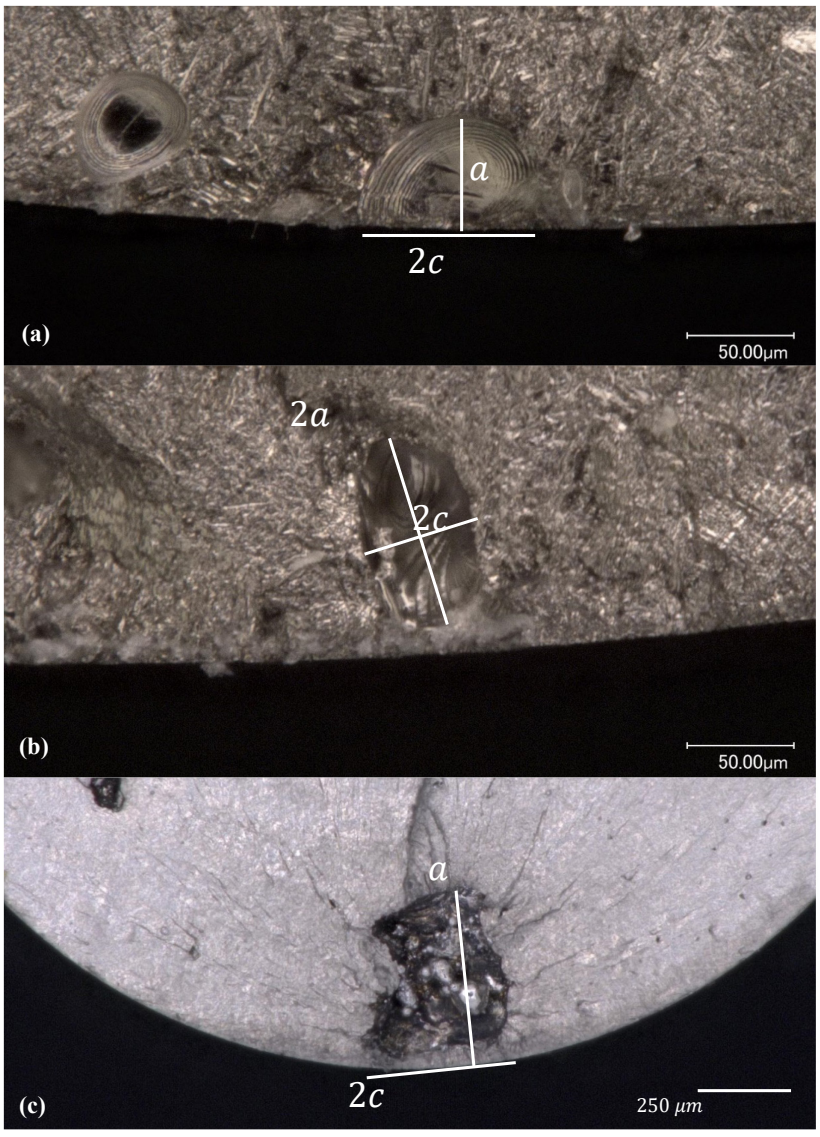

Figure 1: Optical microscope image of the fracture surface of (a) Ti-6Al-4V specimen showing the measurement of the maximum depth, a, and the maximum width along the surface, 2c of the fatigue crack nucleating surface feature (i.e., a surface pore), (b) Ti-6Al-4V specimen showing the measurement of a sub-surface pore (note that the orientation with respect to the surface is not taken into account for sub-surface pores), and (c) AlSi10Mg specimen showing a large sub-surface pore/LoF very close to the surface. For that reason, it is considered as a surface pore/LoF and measured accordingly.

2.0 MATERIALS AND METHODS

2.1 Microstructure and Discontinuities

Round AlSi10Mg tensile and fatigue specimens are produced at NLR using different laser scan strategies to produce specimens with a wider range of porosity [21], [23]. Fabrication was done using an SLM Solutions 280HL system. The test specimens were printed vertically with respect to the build plate. After a 2h 300°C stress relief heat treatment, the test specimens were machined and polished to a final gauge diameter of 3 mm and a reduced section length of 18 mm. Polishing down to $R_a \leq 0.2$ µm was performed to minimize the effect of surface roughness and verified using a profilometer.

Round Ti-6Al-4V tensile and fatigue specimens with three orientations (horizontal, vertical and inclined at 45°) are produced on NLR's SLM Solutions 280HL system using old (OP) and newly optimized parameter settings (NP) to produce specimens with a wider range of porosity. The samples were printed with a slight oversize to be able to machine them to size. After a stress relief heat treatment at 788 °C for 2h in argon atmosphere the specimens were machined and polished to a roughness of $R_a \leq 0.2$ µm. After machining, the Ti-6Al-4V specimens have a diameter of 5 mm and a reduced section length of 30 mm.

All tensile and fatigue specimens have a stress concentration factor close to unity ($K_t \approx 1$). Tensile testing is performed according to ASTM standards, ASTM E8 / E8M - 11. The tensile samples were tested with a 1 mm/min speed on an Instron 5900R test machine with a 100 kN load cell. For fatigue testing a constant amplitude 25 Hz sinusoidal load was introduced by a servo-hydraulic test machine with a 100 kN load cell. A stress ratio, R:

$$R = \frac{S_{min}}{S_{max}} \tag{2}$$

of 0.1 was applied, where S_{min} and S_{max} are the minimum and maximum stress in a loading cycle, respectively. Fractography was carried out with an Optical Microscope (OM) and Scanning Electron Microscope (SEM) after fatigue testing to determine the size of the nucleating discontinuities. The measurements were made on the fracture surface and hence the projected dimensions were measured that were perpendicular to the loading direction.

2.1.1 Fitting Methodology

For a limited number of cycles required for crack nucleation, the fatigue life is equal to the integral of the small and long crack growth rate from the initial crack length to the final crack length [24]. For a given stress ratio, the fatigue crack growth rate follows a power law relationship with the S_{max} [3], [6], [24], [25]. Hence, the fatigue life (N) should have a power law relationship with the S_{max}:

$$N = C^* \cdot S_{max}^{-n} \tag{3}$$

Where n is the power law exponent and C^* contains all the information on crack growth rate, geometry and initial and final crack length. The S-N curve becomes linear when plotted on log-log scale:

$$\log N = -n \log S_{max} + \log C^* \tag{4}$$

All S-N curves in this report will be plotted using the scientific methodology, where the independent variable, (i.e., stress) is on the horizontal axis and the dependent variable (i.e., fatigue life) on the vertical axis. Conventionally, S-N curves are plotted with the cycles to failure on the horizontal axis and stress on the vertical axis. However, standard regression analysis on conventionally plotted S-N curves results in an incorrect slope. This is due to the fact that the stress between the model and data points is minimized instead of the test output N.

The power law exponent, n, between a reference point (S_{ref}, N_{ref}) and the experimental test result of a single fatigue specimen (S, N) can be calculated using the following equations:

$$N = N_{ref}\left(\frac{S}{S_{ref}}\right)^{-n} \tag{5}$$

from which n can be calculated:

$$n = -\frac{\log(N/N_{ref})}{\log(S/S_{ref})} \tag{6}$$

and for a given reference point a set of exponents are determined for all fatigue specimens.

Figure 2 shows S-N data on a log-log scale, as well as different exponents or slopes n between the data points and the reference point. Similarly, as in Ref. [21], it is assumed that the exponent or slope n is a function of the discontinuity size. As indicated, here the equivalent radius is used as discontinuity size and r_{eq} is experimentally determined for each fatigue specimen by fractography and Equation (1).

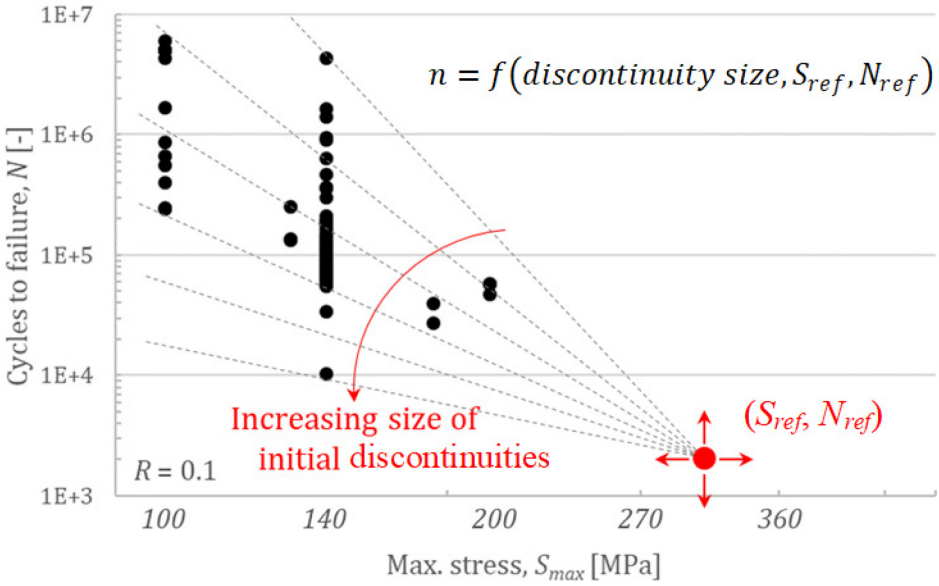

Figure 2: Fatigue life as a function of the maximum stress showing different slopes between the experiment *S-N* data and a reference point (S_{ref}, N_{ref}). It is assumed that the slopes or exponents *n* are a function of the discontinuity size and the reference point.

2.2 Mesostructure

Stretch-dominated multiple load path specimens, consisting of a test section with 9 and 81 cylindrical struts, are designed and manufactured by L-PBF with AlSi10 Mg and Ti-6Al-4V (see Figure 3). The thickness of the cylindrical struts is gradually increased away from the reduced sections to avoid unwanted stress concentrations, and the top and bottom part of the specimens are used for gripping. A specimen with a single strut was also designed and manufactured by L-PBF. All three specimens are designed to have equal cross-sectional areas and equal outer surface areas in the reduced sections, which results in different lengths of the reduced sections. A diameter of 1 mm and a reduced section length of 10 mm were chosen for the specimens

with 81 struts. This results in a diameter of 3 mm and 9 mm for the specimens with three struts and one strut, respectively.

For both materials, all specimens were printed vertically on a single build plate. A 2h, 300°C stress relief heat treatment was applied after the manufacturing of the AlSi10Mg specimens and, a 2h, 788°C stress relief heat treatment in argon atmosphere was applied after the manufacturing of the Ti-6Al-4V specimens.

All specimens were tested in the as-built surface condition at a frequency of 15 Hz at an R of 0.1. Potential drop measurements were performed on the multiple load path specimens to measure damage progression during fatigue testing.

The diameters of the struts were measured with a digital caliper, but due to surface roughness and to shrinkage and the accuracy of the SLM machine, differences in diameter with the specimen design were expected. According to size effects described in literature [26], this effect was expected to be larger for smaller diameters. Hence, non-destructive tensile tests were performed on the multiple load path specimens to measure their stress-strain response and determine the actual cross-sectional area of the specimens.

One AlSi10Mg and one Ti-6Al-4V specimen with 9 struts is cut in 9 single struts, which were fatigue tested individually to investigate the fatigue life distribution of single struts. Additionally, AlSi10Mg single strut specimens with the same diameter (3 mm) and reduced section length (30 mm) were printed vertically to compare the fatigue life with that of the single struts cut from the 9-strut AlSi10Mg specimen. These specimens were also stress relief heat treated and tested in the as-built surface condition.

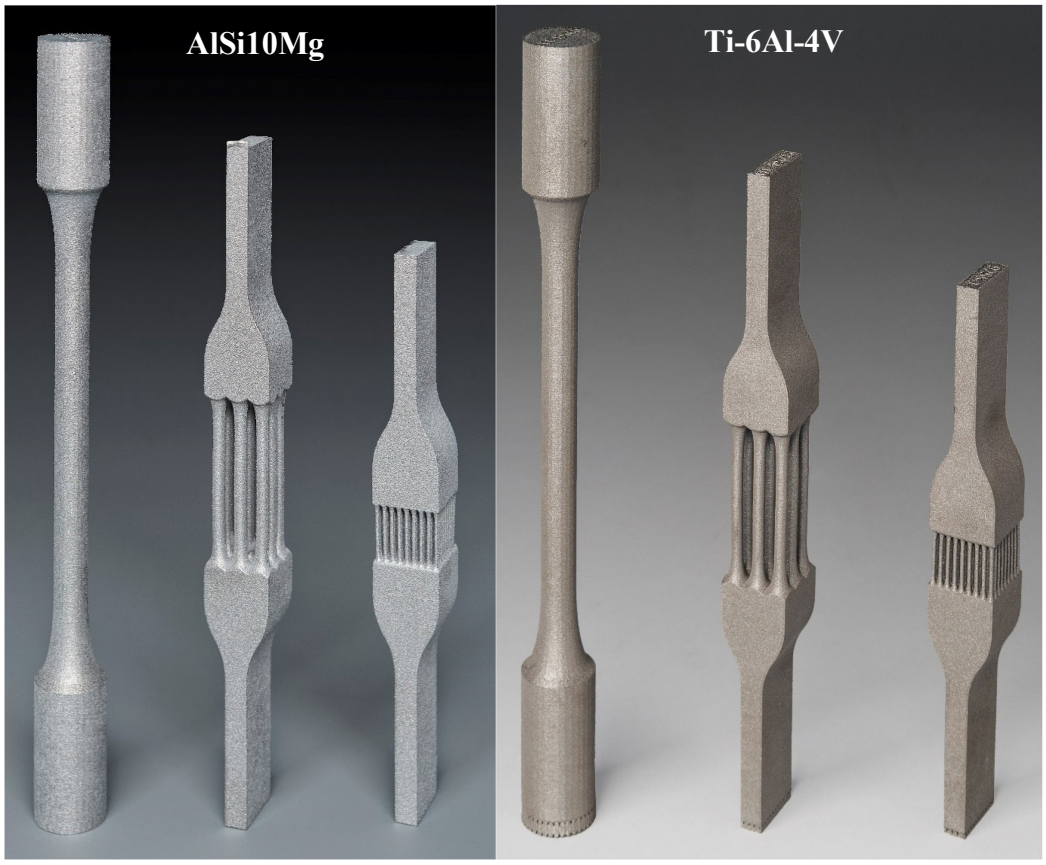

Figure 3: Stretch-dominated multiple load path specimen made by laser powder bed fusion using AlSi10Mg (left) and Ti-6Al-4V (right). All specimens are designed to have equal cross-sectional areas and equal outer surface areas of the reduced sections and were tested in the as-built surface condition.

3.0 RESULTS

3.1 Microstructure and Discontinuities

3.1.1 Tensile Results

Table 1 shows the average and standard deviation of four tensile tests on polished AlSi10Mg specimens and eight tensile tests on polished Ti-6Al-4V specimens for each orientation and set of parameter settings. For AlSi10Mg, the maximum UTS (UTS plus standard deviation) is 247. There are only minor differences between the polished Ti-6Al-4V specimens for each orientation and parameter settings and the maximum UTS is about 1020 MPa.

Table 1: Tensile test results (average and standard deviation).

Material	Orientation	Sy (MPa)	UTS (MPa)	E (GPa)	Elongation (%)
AlSi10Mg	Vertical	131 ± 3	247 ± 0.5	67 ± 5	12 ± 2
Ti-6Al-4V OP	Horizontal	944 ± 7	1012 ± 7	118 ± 3	15.7 ± 0.5
	45°	945 ± 7	1016 ± 4	120 ± 2	16.5 ± 0.7
	Vertical	975 ± 7	1017 ± 3	121 ± 1	16.7 ± 0.2
Ti-6Al-4V NP	Horizontal	950 ± 5	1017 ± 4	117 ± 1	16.4 ± 0.4
	45°	949 ± 8	1014 ± 5	118 ± 2	15.8 ± 0.5
	Vertical	975 ± 7	1018 ± 2	120 ± 1	16.1 ± 0.6

3.1.2 Fatigue Results AlSi10Mg

Figure 4 shows the fatigue life as a function of maximum stress for all polished AlSi10Mg specimens. Fractography showed that for all specimens that failed, the fatigue cracks nucleated from pores located at the surface or sub-surface, as indicated in the figure. The pores are quite large, ranging from an r_{eq} from roughly 50 µm to 500 µm, have irregular shapes and show unmelted powder particles (see Figure 1). Hence, these pores are better considered to be LoF defects rather than gas pores. Figure 5 shows the power law exponent, n, as a function of the equivalent radius, r_{eq}, for crack nucleation from (surface) pores/LoF and sub-surface pores/LoF for the AlSi10Mg specimens. The exponents, n, are dependent on the coordinates of the pivot point (S_{ref}, N_{ref}). For Figure 5 the coordinates (247 MPa, 6959 cycles) have been used. The relationship between the exponents and the equivalent radius can be described by a power law:

$$n = C_1 r_{eq}^{-C_2} \tag{7}$$

where C_1 and C_2 are parameters that apply for a set of data and are experimentally determined. For the specimens that failed from surface pores C_1 and C_2 are 42.5 and 0.406, respectively. The value for C_2 is close to that obtained for corrosion pits over a wide range of r_{eq} [27]. The number of data points and the range of r_{eq} is small for the sub-surface pores/LoF defects. Therefore, the C_2 of the surface pores is used and only C_1 for the sub-surface pores/LoF is determined for a given reference point. The results of four specimens indicated with an x are omitted from the fitting procedure, because with the least squares regression analysis the outliers have a huge effect on the fit parameters while the purpose of the regression analysis is to determine the general trend of the majority of the data points. Although the outliers are not used for regression analysis, the data points are still shown in all figures.

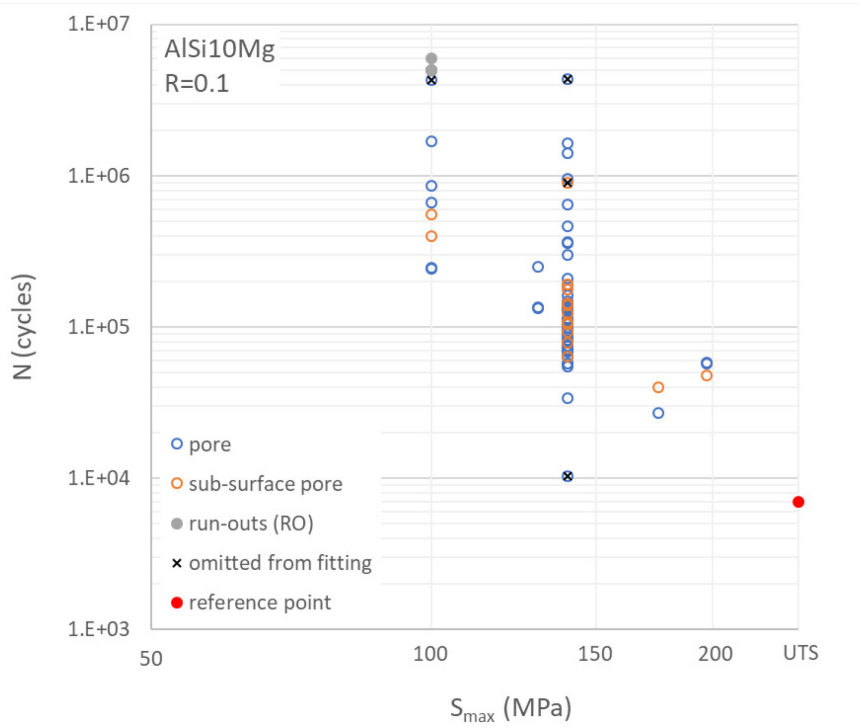

Figure 4: Fatigue life as a function of the maximum stress for all polished AlSi10Mg specimens. The results from fractography are already incorporated in this graph. The results of four specimens indicated with an x are omitted from the outlined fitting procedure.

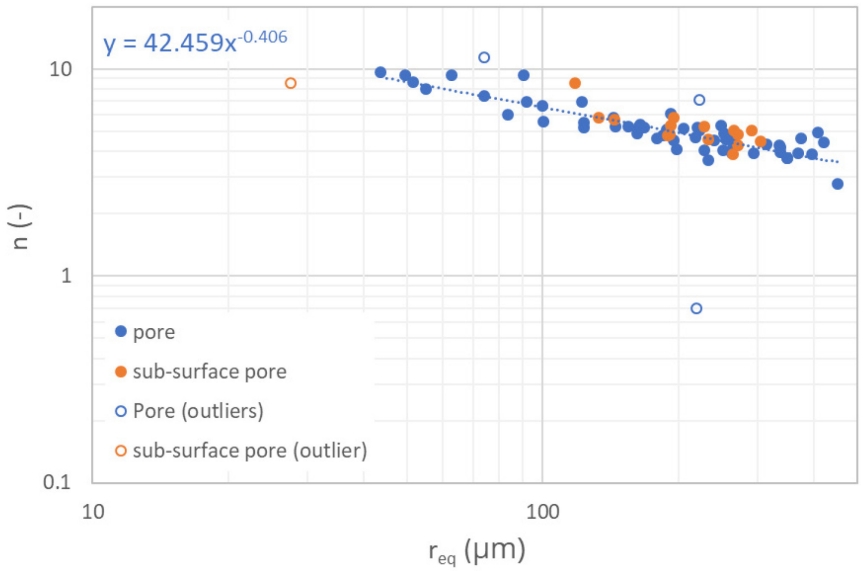

Figure 5: Power law exponent, n, as a function of the equivalent radius, r_{eq}, for all AlSi10Mg specimens (including the four outliers, which were not used for fitting) and reference point (247 MPa, 6959 cycles).The data is fitted using Equation (7).

Figure 6 shows the AlSi10Mg fatigue life for pores and sub-surface pores as a function of the predicted number of cycles, which is calculated using the reference point and by substituting Equation (7) into Equation (5):

$$N_{pred} = N_{ref}\left(\frac{S_{max}}{S_{ref}}\right)^{-C_1 r_{eq}^{-C_2}} \tag{8}$$

When the coordinates of the reference point are changed, C1 and C2 are automatically determined from the experimental data, as shown in Figure 5. The reference point can be changed, as indicated in Figure 2, until a proportional (linear) relationship between the measured and predicted fatigue life is reached (see Figure 6). A boundary condition for the reference point is imposed which limits the maximum value of the reference stress to the maximum UTS (UTS plus standard deviation). Figure 6 shows that a proportional relationship, with the proportionality constant of 1.007, which is closest to unity that could be reached, is obtained for a reference point of (247 MPa, 6959 cycles). Since the maximum UTS is 247 MPa, the reference point becomes (UTS, 6959 cycles) and it is shown in Figure 4 as well.

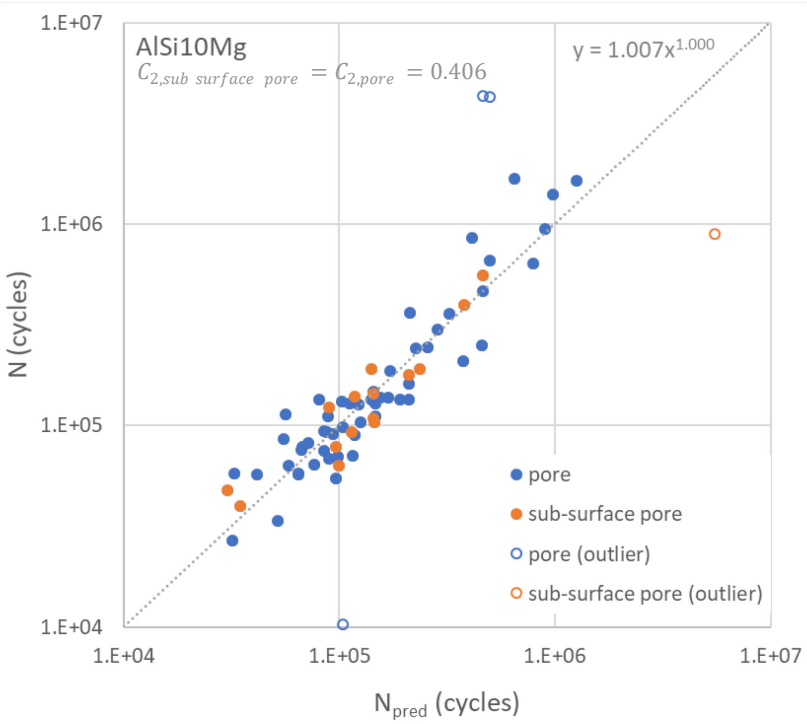

Figure 6: Fatigue life as a function of the predicted number of cycles for all AlSi10Mg samples (including the four outliers, which were not used for fitting) and reference point (247 MPa, 6959 cycles).

3.1.3 Fatigue Results Ti-6Al-4V

Figure 7 shows the fatigue life as a function of stress for all polished Ti-6Al-4V specimens manufactured with old parameters (OP) and new parameters (NP). The fatigue lives of the NP specimens are similar to those of the OP specimens, but they are tested at higher maximum stresses. Fractography showed that the optimized parameter settings (NP) result in less failures from pores compared to the old parameter settings (see Figure 7). The pores from which the fatigue cracks nucleate in both the OP and NP specimens are shiny and spherical, indicating that they can be classified as gas pores. The NP specimens show fewer failures from pores and other fatigue crack nucleating discontinuities or features, such as machine marks, are observed.

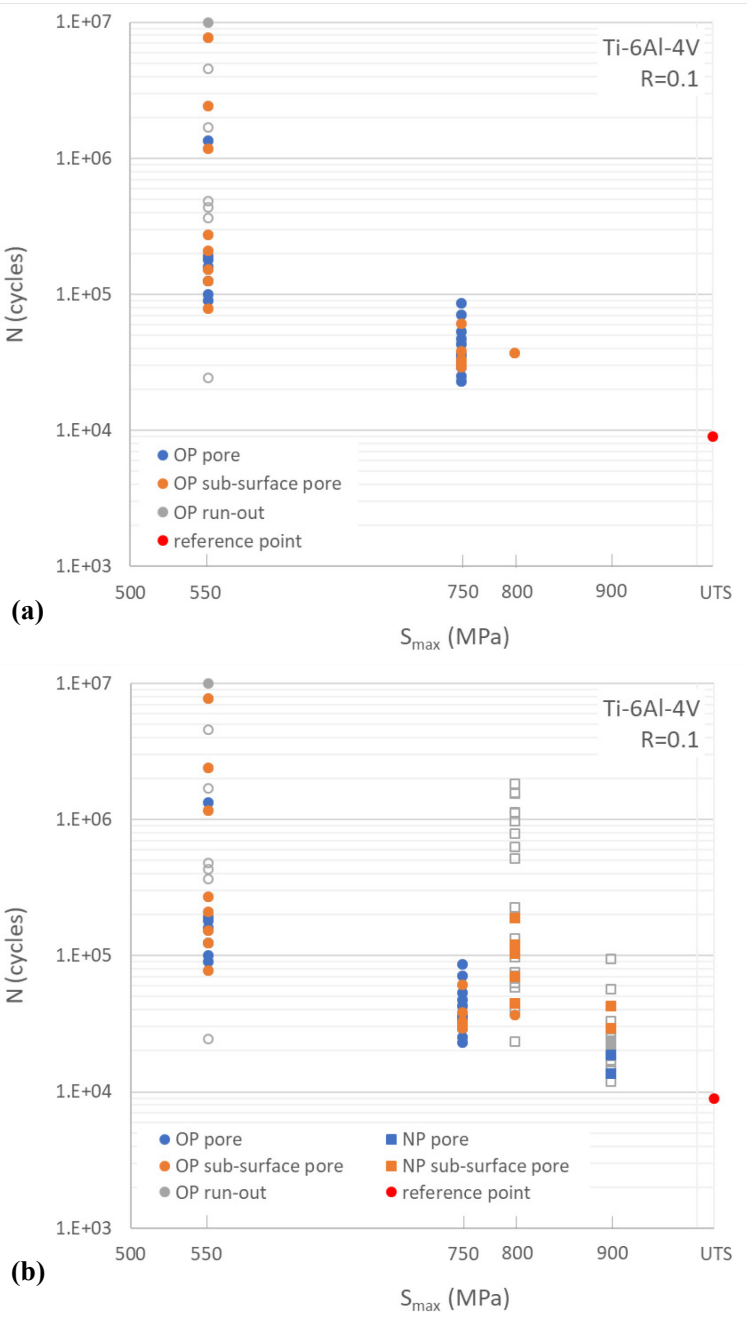

Figure 7: Fatigue life as a function of the maximum stress for all polished Ti-6Al-4V specimens manufactured with (a) old parameters (OP) and (b) new parameters (NP). In figure (b) the OP specimens are shown as well and the results from fractography are already incorporated in this graph. The blue data points represent specimens that failed from (surface) pores, the orange for sub-surface pores and the open data points correspond to other types of fatigue crack nucleating discontinuities or features.

Since the size of these discontinuities cannot be accurately quantified, or there are too few of similar discontinuities to determine C_1 and C_2, only the (surface) gas pores and sub-surface gas pores are used to obtain C_1 and C_2 in Equation (7). Figure 8 shows the power law exponent, n as a function of the equivalent radius, r_{eq} for crack nucleation from (surface) pores and sub-surface pores. The values of C_2 are about 0.4 for all data sets, except for the two NP specimens that failed from surface pores. The exponents, n, for the NP sub-surface

pores are higher compared to the OP sub-surface pores, which results in a higher C_1 for the NP specimens. Since the value of C_1 is dependent on the value of C_2 and most data sets show a limited range of r_{eq}, the C_2 value from the data set with the widest range (OP pore specimens) is used obtain C_1 for all four data sets.

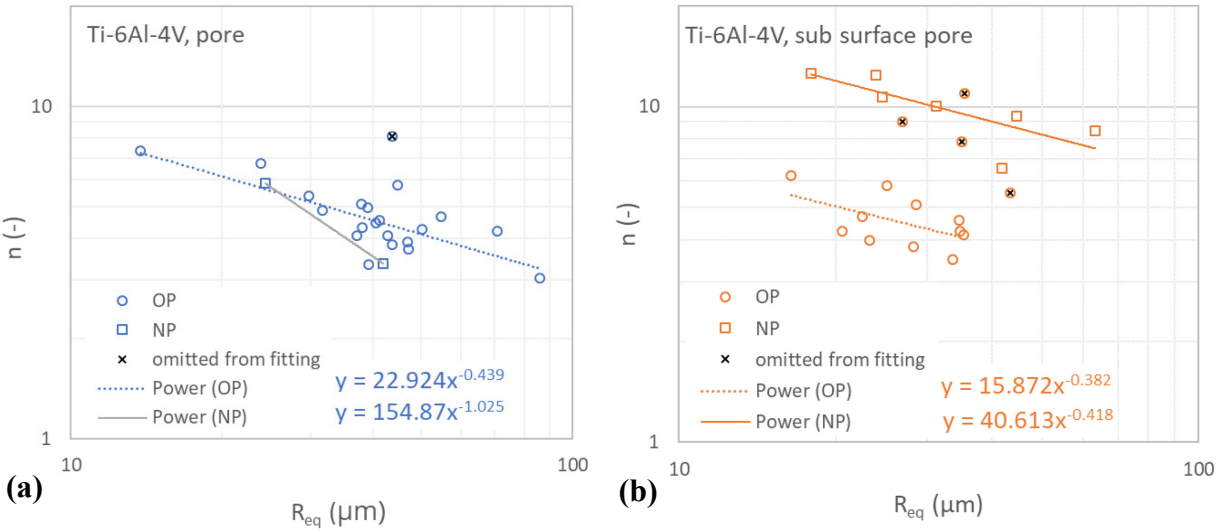

Figure 8: Power law exponent, n, as a function of the equivalent radius, r_{eq}, for the Ti-6Al-4V specimens that failed from (a) (surface) pores and (b) sub-surface pores. Both graphs include the outliers that were not used for fitting. The reference point (1,020 MPa, 9,005 cycles) was used to create the data, which is fitted using Eq. (7) for the OP and NP specimens.

Figure 9 shows the Ti-6Al-4V fatigue life for pores and sub-surface pores as a function of the predicted number of cycles. For the specimens that failed from surface pores a proportional relationship with the proportionality constant of 1.00 is obtained for a reference point of (1,020 MPa, 9,005 cycles). Since the maximum UTS is 1,020 MPa, the reference point becomes (UTS, ,9005 cycles) and it is shown in Figure 7 as well. For this reference point the C_2 for the OP pore specimens is 0.439 and this value has been used to obtain C_1 for all Ti-6Al-4V data sets. For the same reference point also a proportional relationship with the proportionality constant close to unity is obtained for the specimens that failed from sub-surface pores.

3.2 Mesostructure

3.2.1 Fatigue Results AlSi10Mg

Figure 10(a) shows the *S-N* curves for the AlSi10Mg multiple load path specimens with 81 struts and nine struts, and the single strut specimen with the same cross-sectional area and the same surface area in the as-built surface condition. All three curves have a similar slope, but the fatigue lives of the 9-strut specimens are lower than the single strut, and the 81-strut specimens are lower than the 9-strut specimens. Figure 10(b) shows the results of Figure 10(a) at a maximum stress of about 140 MPa and includes the results from the nine single struts cut from a 9-strut specimen and individually printed single strut specimens with the same diameter (3 mm) and reduced section length (30 mm). The 9-strut specimens have a log average fatigue life of 59 kcycles. The 9 single struts cut from a 9-strut specimen have similar fatigue lives with a log average of 63 kcycles, but a larger variability. However, the individually printed single strut specimens with a diameter of 3 mm have a similar fatigue life as the single struts with a diameter of 9 mm. The log average fatigue life of the individually printed 3 mm and 9 mm specimens is 98 kcycles and 113 kcycles, respectively. Figure 10(b) shows that the variability in fatigue lives on log scale is similar for the individually printed 3 mm and 9 mm specimens as well as for the nine single struts cut from a 9-strut specimen.

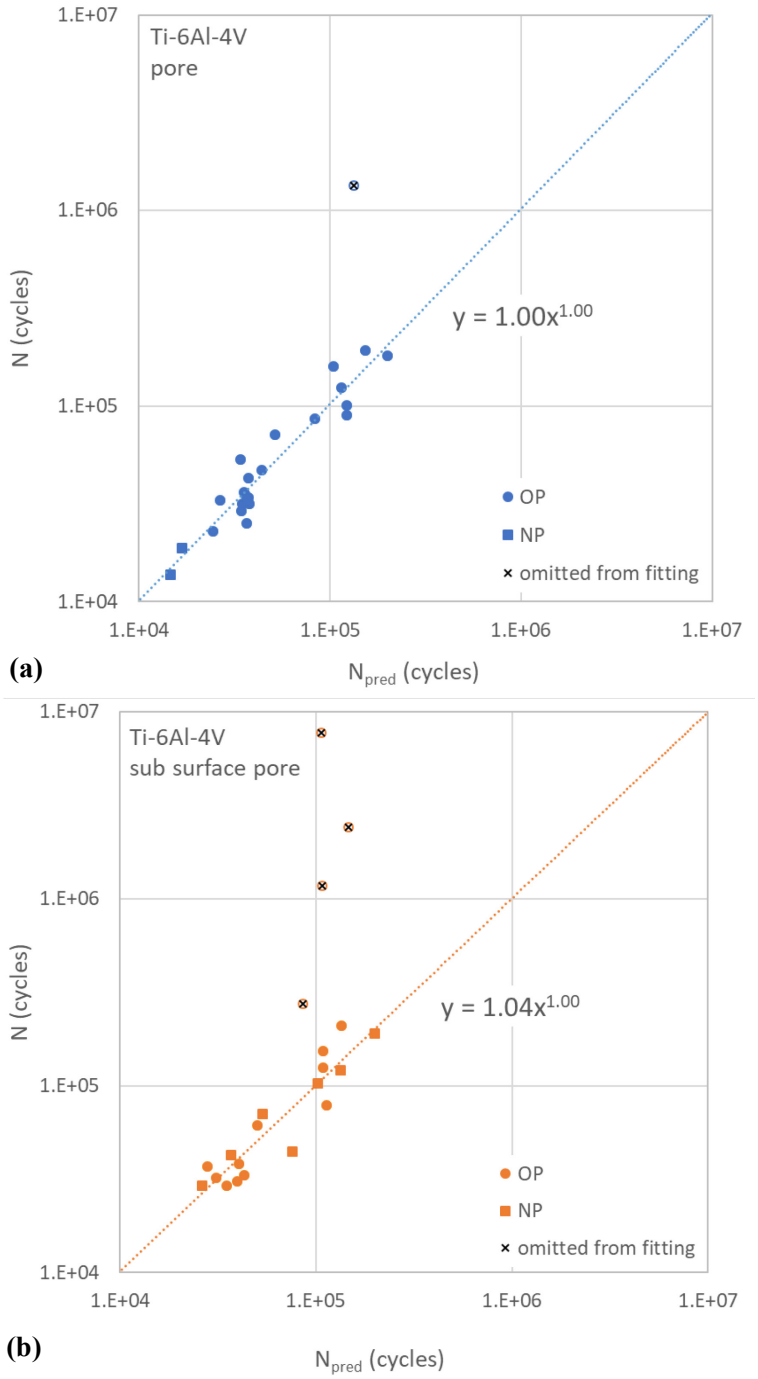

Figure 9: Fatigue life as a function of the predicted number of cycles for the Ti-6Al-4V samples that failed from (a) pores and (b) sub-surface pores. The reference point (1020 MPa, 9005 cycles) and C_2 = 0.439 was used for all four data sets. The outliers are shown but were not used for fitting.

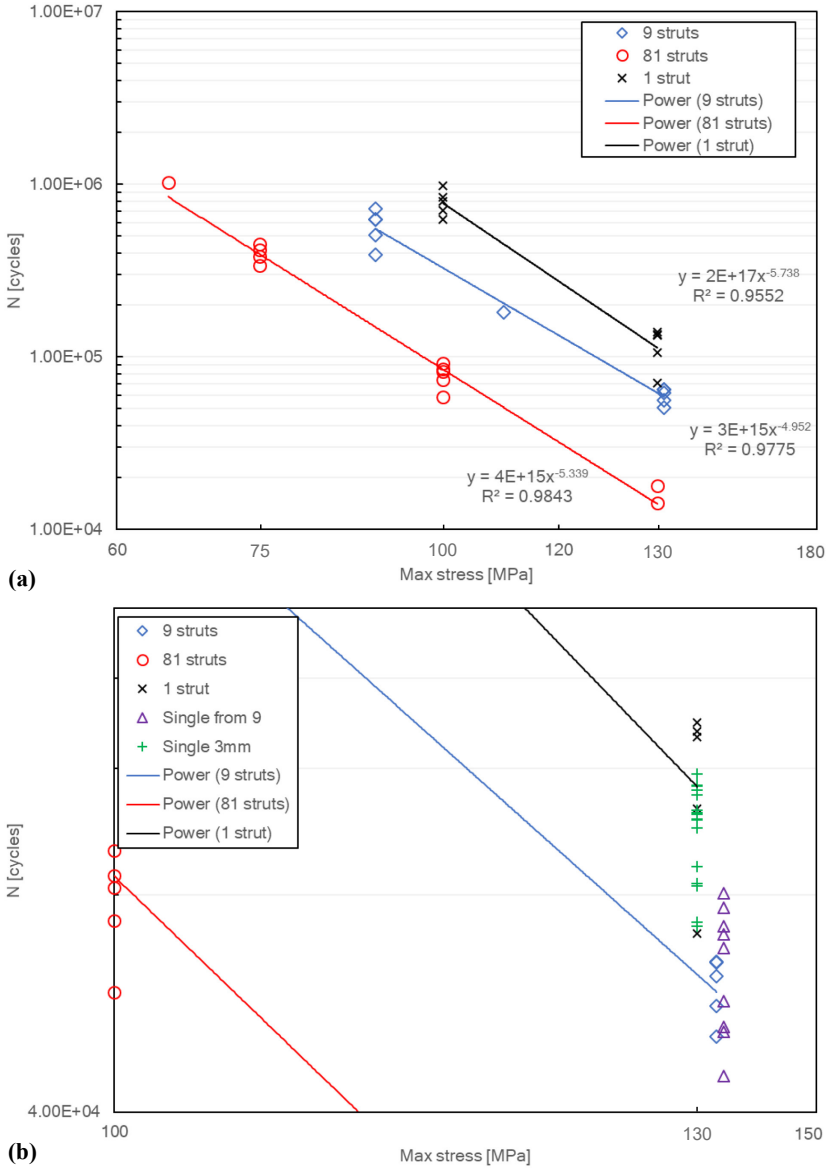

Figure 10: (a) Fatigue life as a function of the maximum stress for the AlSi10Mg multiple load path specimens with 1, 9 and 81 struts. (b) Detail of figure (a) with the results of the single struts cut from a 9-strut specimen and the 3 mm diameter specimens that were printed individually.

3.2.2 Fatigue Results Ti-6Al-4V

Figure 11(a) shows the *S-N* curves for the Ti-6Al-4V multiple load path specimens with 81 and 9 struts and the single strut specimen, with the same cross-sectional area and the same surface area in the as-built surface condition. All three curves have a similar slope; however, similar to the AlSi10Mg specimens, the fatigue lives of the 9-struts specimens are lower than those of the single strut and the 81-struts specimens are lower than those of the 9-struts specimens. The results of 18 single struts cut from two 9-strut specimens are included as well, but these specimens were only tested at a single stress level of 320 MPa. Figure 11(b) shows the result at a maximum stress of 320 MPa for the four different types of specimens. The log average of the 1-strut 9 mm, 1-strut 3 mm, 9-strut and 81-strut specimens are 156, 74, 72 and 37 kcycles, respectively. The variability of the 9-strut specimens is much less than that of the 18 single struts cut from two 9-strut specimens. The potential drop measurements show that failure of the multiple load path 9-strut specimens starts with failure of a single strut

about 5–10 kcycles before failure of the entire specimen, followed by sequential failure of 2–5 struts just prior to final overload in the remaining struts. For the 81-strut specimens failure of the first strut occurs about 10–15 kcycles prior to failure of the entire specimen by overload when about 20-30 struts have sequentially failed.

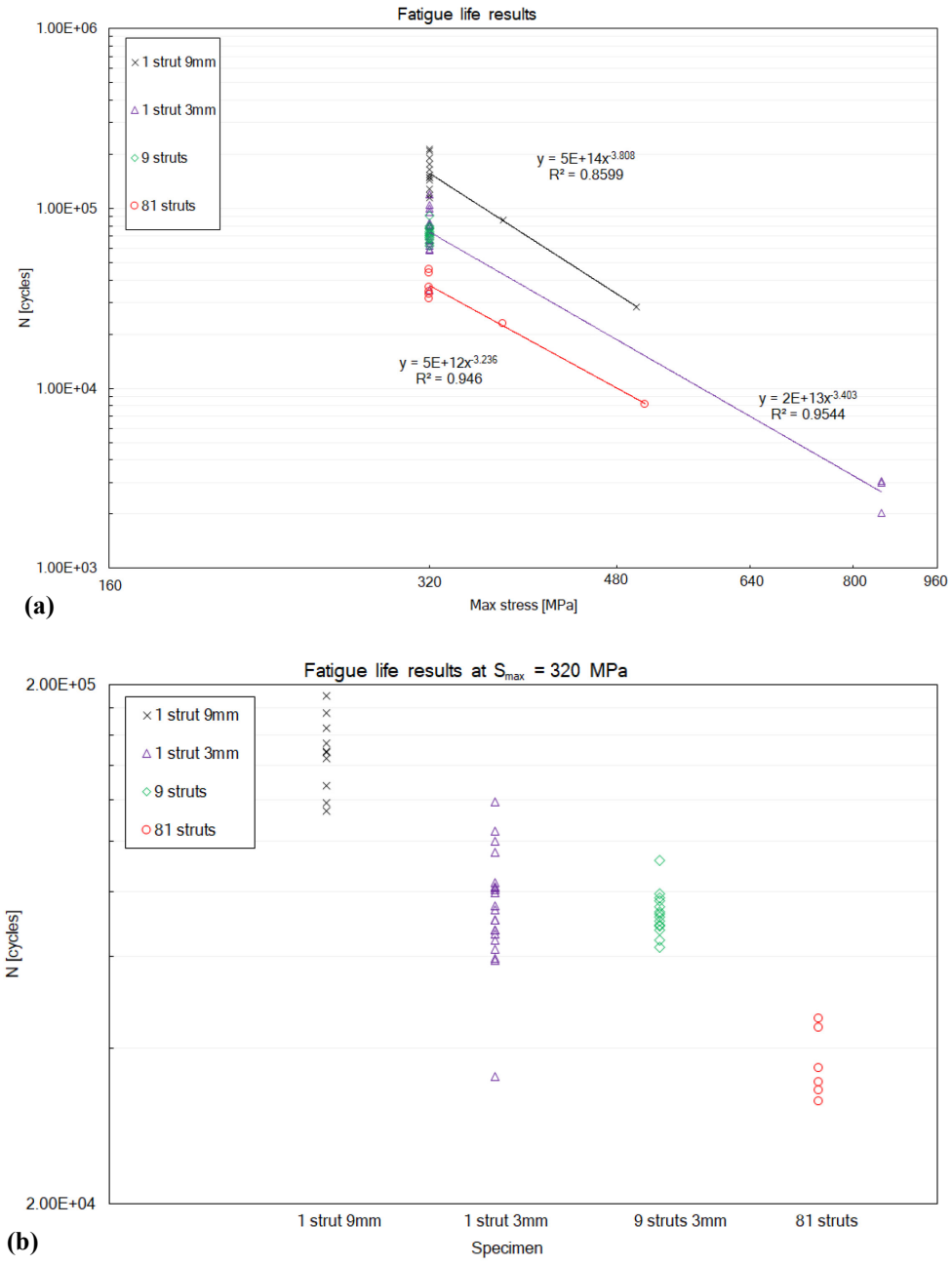

Figure 11: Fatigue life as a function of the maximum stress for the Ti-6Al-4V multiple load path specimens with 1, 9 and 81 struts and the results of the single struts cut from two 9-strut specimen. (b) Overview of the fatigue life results at S_{max} = 320 MPa.

4.0 DISCUSSION

4.1 Microstructure

For the sub-surface pores/LoF defects in the AlSi10Mg specimens the C_1 is slightly higher than for surface pores/LoF defects. Although there is a narrow range of r_{eq} for the sub-surface pores/LoF, C_2 appears to follow the same trend as for the surface pores/LoF. A higher C_1 basically means a higher exponent n for the entire data set, hence a higher fatigue life for a given r_{eq}. It is expected that a crack like defect has a lower fatigue life compared to a spherical pore with the same area perpendicular to the load. Semi-spherical surface pores with the same radius as sub-surface or interior spherical pores have lower fatigue lives compared to interior spherical pores, because the crack grows in a vacuum first. This results in higher fatigue crack growth rates in air as compared to vacuum and hence the fatigue life decreases for defects with the same radius when located at the surface. Thus, it is likely that the initial crack growth from the sub-surface pore to the surface is slower and takes additional cycles compared to a surface pore with a similar r_{eq}. The value of C_2 for the surface and sub-surface gas pores in Ti-6Al-4V is similar to that of the LoF porosity in AlSi10Mg. A similar value is obtained for corrosion pits in aluminium alloy 7075-T7351 plate material [27]. As a result, it is expected that different types of discontinuities have a similar behaviour and a similar value of C_2. The OP and NP sub-surface pores in Ti-6Al-4V have different values of C_1 (see Figure 8). Hence, it is expected that the effect of microstructure, discontinuity shape and location is incorporated in the value of C_1. Consequently, all data can be fitted using the general equation with an average value of 0.42 for C_2:

$$N_{pred} = N_{ref}\left(\frac{S_{max}}{UTS}\right)^{-C_1 r_{eq}^{-0.42}} \tag{9}$$

where the value of C_1 is experimentally determined for each type of material microstructure and discontinuity using the experimental data and N_{ref}. Therefore, N_{ref} is the only fit parameter for a given material. Since the projected discontinuity size is measured perpendicular to the loading direction and the maximum UTS is similar for all three orientations, the orientation of the Ti-6Al-4V specimens does not have an additional influence.

4.2 Mesostructure

The results from the multiple load path specimens show that failure of a single strut occurs first. However, the specimens do not fail; instead, the load is transferred to the remaining struts, which are able to sustain that load. It is likely that the remaining struts already have fatigue damage, and the increased load on the remaining struts accelerates the fatigue crack growth rate in those struts. This quickly leads to failure of additional struts until the net-section stress in the remaining struts exceeds the UTS of the material, resulting in final failure by overload. Since failure of the specimen does not occur immediately after the failure of the first strut, the fatigue life of the multiple load path specimens is less sensitive to single struts with significantly lower fatigue life. On the other hand, having more struts increases the chance of encountering a strut with a lower fatigue life. This combined behaviour results in less variability between the multiple load path specimens compared to the variability in the fatigue life of the single struts obtained from these specimens as observed for both materials (see Figure 10(b) and Figure 11(b)). The load transfer after failure of the first struts likely results in a slightly lower log average fatigue life for the multiple load path 9-strut specimens compared to the single struts obtained from these specimens; 59 vs 63 kcycles for AlSi10Mg and 72 vs 74 kcycles for Ti-6Al-4V. Therefore, the multiple load path specimens can be considered damage tolerant and reflect the average fatigue life of the individual members of the multiple load path structure.

The individually printed single strut AlSi10Mg specimens with diameters of 3 and 9 mm have similar fatigue lives of 98 and 113 kcycles, respectively. Failure by fatigue occurs through crack growth, with crack growth rates becoming quite high just prior to specimen failure. Therefore, it is expected that the effect of the specimen diameter is limited for this difference in diameter, which corresponds to the results.

However, the fatigue lives of the single struts cut from the 9-strut specimens have a lower fatigue life compared to the individually printed single strut specimens. The same applies to Ti-6Al-4V, even though no individual printed specimens with 3 mm diameter were manufactured and only specimens with a 9 mm diameter were produced. Hence, there is a difference between individually printed struts and those in a multiple load path configuration. Since the multiple load path specimens reflect the average behaviour of the individual members, it is likely that the effect becomes more pronounced with an increase in the number of struts and a decrease in their thickness, as indicated by the lower fatigue lives of the 81-strut specimens for both materials. The effect could come from a difference in scan strategy when printing single struts versus struts in a multiple load path specimen, or it could result from small differences in geometry, as the struts cut from the 9-strut specimens appeared slightly curved. This curvature could introduce bending in the specimen, leading to localized stress increases.

Differences in scan strategy can result in variations in microstructure and porosity distribution due to different cooling rates. The surface roughness-to-diameter ratio is not expected to have a significant effect, as the individually printed 3 mm AlSi10Mg specimens should have a similar surface roughness-to-diameter ratio to the 3 mm struts obtained from the 9-strut specimens, unless the difference in scan strategy also results in a different surface roughness-to-diameter ratio. Also, the stress-strain response of all specimen types was measured to determine the stiffness of the specimen types and hence the load bearing area. The load bearing area was used to determine the stress in the different specimen types, rather than using the diameter measured externally with a digital calliper, which includes the surface roughness. While bending is expected to be the main factor contributing to the decrease in fatigue life for the structural members of the multiple load path specimens, other contributing factors from differences in scan strategy, such as increased porosity for thinner struts and its effect on fatigue life, as demonstrated in the previous section, could not be excluded and require further investigations.

5.0 CONCLUSIONS

Multi-disciplinary design optimization and novel manufacturing technologies like additive manufacturing have provided designers with tools to create highly optimized structures as well as the ability to fabricate them. The introduction of ICME and hierarchical bioinspired architected materials require relationships between the microstructure and mesostructure of materials and the performance of materials in terms of failure mechanisms (e.g., fatigue). The microstructure determines the mechanical properties, and the distribution of discontinuities is a component of the material's microstructure. It has been shown that the effect of the UTS and projected discontinuity size on the fatigue life can be modelled with a relationship that contains only one fit parameter (i.e. N_{ref}), which can be regarded as the fatigue life at the UTS. Fracture mechanics considerations have been used to define a single metric for the projected size of the discontinuity (i.e. r_{eq}), the radius of a semi-circle of equal area as the projected semi-elliptical size of a discontinuity. It is expected that the remaining differences between the experimental and predicted fatigue life by Equation (9) are due to differences in the 3D shape of a discontinuity and variations in small crack growth rates surrounding a discontinuity. The stretch-dominated multiple load path specimens show that the effect of the mesostructure results in a more damage tolerant design, where the multiple load path specimens show less variability in fatigue life than the individual members of the structure. However, the results also show increasing the number of load paths and decreasing the load path diameter for additively manufactured specimens decreases the fatigue life of the individual members. Therefore, for a multiple load path specimen of equal cross-sectional area as a single load path specimen the variability in fatigue life decreases for increasing the number of load paths. However, the fatigue life itself decreases as well resulting in lower fatigue lives of the multiple load path specimen compared to the lowest fatigue life of the single load path specimen of equal cross-sectional area. The latter could result from slight bending in the structural members of the multiple load path specimens, but contributing factors from differences in scan strategy could not be excluded and require further investigations.

6.0 REFERENCES

[1] Tammas-Williams, S., Withers, P.J., Todd, I., and Prangnell, P.B. "The Influence of Porosity on Fatigue Crack Initiation in Additively Manufactured Titanium Components," Sci Rep, vol. 7, no. 1, 7308, Dec 2017. doi: 10.1038/s41598-017-06504-5

[2] Romano, S., Brückner-Foit, A., Brandão, A., Gumpinger, J., Ghidini, T., and Beretta, S. "Fatigue Properties of AlSi10Mg Obtained by Additive Manufacturing: Defect-Based Modelling and Prediction of Fatigue Strength," Engineering Fracture Mechanics, vol. 187, 165-189, Jan. 2018. doi: 10.1016/j.engfracmech.2017.11.002

[3] Amsterdam, E., Wiegman, J.W.E., Nawijn, M., and De Hosson, J. Th. M. "The Effect of Crack Length and Maximum Stress on the Fatigue Crack Growth Rates of Engineering Alloys," International Journal of Fatigue, 161, 106919, 2022. doi: 10.1016/j.ijfatigue.2022.106919

[4] Persenot, T. Burr, A., Dendievel, D. Buffiere, J.-Y., Maire, E., Lachambre, J. et al. "Fatigue Performances of Chemically Etched Thin Struts Built by Selective Electron Beam Melting: Experiments and Predictions," Materialia, 9, 100589, Mar 2020. doi: 10.1016/j.mtla.2020.100589

[5] McMurtrey, M.D., Mills, D.E., and Burns, J.T. "The Effect of Pit Size and Density on the Fatigue Behaviour of a Pre-Corroded Martensitic Stainless Steel," Fatigue Fract Eng Mater Struct, 42(1), 3-18, Jan 2019. doi: 10.1111/ffe.12860

[6] Amsterdam, E., Wiegman, J.W.E., Nawijn, M., and Hosson, J.T.M.D. "From Small Crack Growth to Fatigue Life," in "Physics of Failure for Military Platform Critical Subsystems," NATO STO technical report STO-TR-AVT-356, 1-19, NATO Science & Technology Organization, Neuilly-sur-Seine, France, 2021.

[7] Murakami, Y., Takagi, T., Wada, K., and Matsunaga, H. "Essential Structure of S-N Curve: Prediction of Fatigue Life and Fatigue Limit of Defective Materials and Nature of Scatter," International Journal of Fatigue, 146, 106138, May 2021. doi: 10.1016/j.ijfatigue.2020.106138

[8] Murakami, Y., Kawakami, K., and Duckworth, W. "Quantitative Evaluation of Effects of Shape and Size of Artificially Introduced Alumina Particles on the Fatigue Strength of 1.5Ni-Cr-Mo (En24) Steel," International Journal of Fatigue, 13(6), 489-499, Nov 1991. doi: 10.1016/0142-1123(91)90485-H

[9] Murakami, Y. and Endo, M. "Effects of Defects, Inclusions and Inhomogeneities on Fatigue Strength," International Journal of Fatigue, 16(3), 163-182, Apr 1994. doi: 10.1016/0142-1123(94)90001-9

[10] Harmsworth, C.L. "Effect of Corrosion on the Fatigue Behavior of 2024-T4 Aluminum Alloy," USAF, ASD Technical Report 61-121, 1961.

[11] Dolley, Lee, and Wei, "The Effect of Pitting Corrosion on Fatigue Life," Fat Frac Eng Mat Struct, 23(7)7, 555-560, Jul 2000. doi: 10.1046/j.1460-2695.2000.00323.x

[12] N.E.C. Co and Burns, J.T. "Effects of Macro-Scale Corrosion Damage Feature on Fatigue Crack Initiation and Fatigue Behavior," International Journal of Fatigue, 103, 234-247, Oct 2017. doi: 10.1016/j.ijfatigue.2017.05.028

[13] Xu, S. and Wang, Y. "Estimating the Effects of Corrosion Pits on the Fatigue Life of Steel Plate Based on the 3D Profile," International Journal of Fatigue, 72, 27-41, Mar 2015. doi: 10.1016/ j.ijfatigue.2014.11.003

[14] Schönbauer, B.M., et al. "Fatigue life estimation of pitted 12% Cr steam turbine blade steel in different environments and at different stress ratios," International Journal of Fatigue, vol. 65, pp. 33–43, Aug. 2014, doi: 10.1016/j.ijfatigue.2013.10.003

[15] Schönbauer, B.M., Stanzl-Tschegg, S.E., Perlega, A., Salzman, R.N., Rieger, N.F. Zhu, S. et al. "The Influence of Corrosion Pits on the Fatigue Life of 17-4PH Steam Turbine Blade Steel," Engineering Fracture Mechanics, 147, 158-175, Oct 2015. doi: 10.1016/j.engfracmech.2015.08.011

[16] Zhou, S. and Turnbull, "Influence of Pitting on the Fatigue Life of a Turbine Blade Steel," Fat Frac Eng Mat Struct, 22(12), 1083-1093, Dec 1999. doi: 10.1046/j.1460-2695.1999.00226.x

[17] McKelvey, S.A. and Fatemi, A. "Surface Finish Effect on Fatigue Behavior of Forged Steel," International Journal of Fatigue, 36(1), 130-145, Mar 2012. doi: 10.1016/j.ijfatigue.2011.08.008

[18] Pegues, J.W., Shamsaei, N., Roach, M.D., and Williamson, R.S. "Fatigue Life Estimation of Additive Manufactured Parts in the As-Built Surface Condition," Mat Design & Process Comms, 1(3), Jun 2019. doi: 10.1002/mdp2.36

[19] Bannantine, J.A., Comer, J.J. and Handrock, J.L. Fundamentals of Metal Fatigue Analysis. Englewood Cliffs, N.J: Prentice Hall, 1990.

[20] Lee, Y.-L., Ed., Fatigue Testing and Analysis: Theory and Practice. Amsterdam ; Boston: Elsevier Butterworth-Heinemann, 2005.

[21] Wits, W.W. and Amsterdam, E. "Fatigue Prediction and Life Assessment Method for Metal Laser Powder Bed Fusion Parts," CIRP Annals, 72(1), 129-132, 2023. doi: 10.1016/j.cirp.2023.03.011

[22] David, L. and Lazarus, V. "On the Key Role of Crack Surface Area on the Lifetime of Arbitrarily Shaped Flat Cracks," International Journal of Fatigue, 154, 106512, Jan 2022. doi: 10.1016/j.ijfatigue. 2021.106512

[23] Wits, W.W., Scolaro, E., Amsterdam, E., and Clare, A.T. "The Role of Scan Strategies in Fatigue Performance for Laser Powder Bed Fusion," CIRP Annals, 71(1), 185-188, 2022. doi: 10.1016/j.cirp.2022.03.006

[24] Amsterdam, E., Nawijn, M., Grooteman, F.P., and Bos, M.J. "Variable Amplitude Fatigue Life Methodology for a Structural Digital Twin," in STO-MP-AVT-369 Digital Twin Technology Development and Application for Tri-Service Platforms and Systems, Båstad, Sweden: NATO Science & Technology Organization, Neuilly-sur-Seine, Oct 2023.

[25] Amsterdam, E., Wiegman, J.W.E., Nawijn, M., and De Hosson, J.H.M. "On the Strain Energy Release Rate and Fatigue Crack Growth Rate in Metallic Alloys," Engineering Fracture Mechanics, 286, 109292, 2023.

[26] Barba, D., Alabort, C., Tang, Y.T., Viscasillas, M.J., Reed, R.C., and Alabort, E. "On the Size and Orientation Effect in Additive Manufactured Ti-6Al-4V," Materials & Design, 186, 108235, Jan 2020, doi: 10.1016/j.matdes.2019.108235

[27] Amsterdam, E. "On the Structure of the S-N Curve: A Universal Model for the Fatigue Life of Engineering Alloys," To be submitted.